IEEE Photonics Journal
An IEEE Photonics Society Publication

Optical Retroreflective Marker Fabricated on Silicon-On-Insulator

Volume 3, Number 5, October 2011

K. Van Acoleyen, Student Member, IEEE
D. C. O'Brien, Member, IEEE
F. Payne
W. Bogaerts, Member, IEEE
R. Baets, Fellow, IEEE

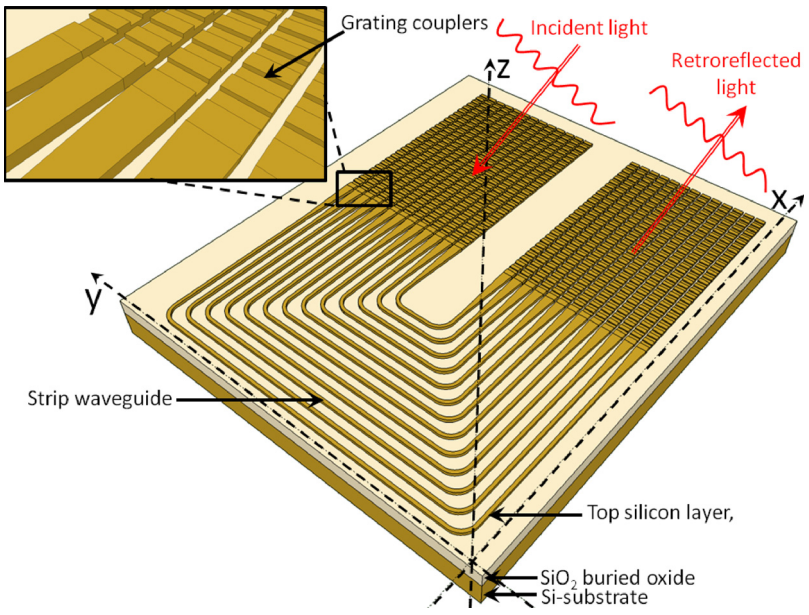

DOI: 10.1109/JPHOT.2011.2164783
1943-0655/$26.00 ©2011 IEEE

Optical Retroreflective Marker Fabricated on Silicon-On-Insulator

K. Van Acoleyen,[1,2] *Student Member, IEEE*, D. C. O'Brien,[3] *Member, IEEE*, F. Payne,[3] W. Bogaerts,[1,2] *Member, IEEE*, and R. Baets,[1,2] *Fellow, IEEE*

[1]Photonics Research Group, Department of Information Technology (INTEC), Ghent University-IMEC, 9000 Ghent, Belgium
[2]Center for Nano- and Biophotonics (NB-Photonics), Ghent University, 9000 Ghent, Belgium
[3]Department of Engineering Science, OX1 3PJ Oxford, U.K.

DOI: 10.1109/JPHOT.2011.2164783
1943-0655/$26.00 ©2011 IEEE

Manuscript received June 30, 2011; revised August 4, 2011; accepted August 5, 2011. Date of publication August 15, 2011; date of current version September 6, 2011. This work was supported by the Methusalem project "Smart Photonic ICs" of Ghent University and the Interuniversity Attraction Poles (IAP) project Photonics@be. Corresponding author: K. Van Acoleyen (e-mail: karel.vanacoleyen@intec.ugent.be).

Abstract: Optical retroreflective markers provide a strong return signal when illuminated by a source, resulting in an easy way to localize and identify an object. As current optical retroreflectors are typically bulky, we have investigated the use of the integrated silicon photonics platform to fabricate optical retroreflectors. An optical retroreflective marker with a total field of view (FOV) of about $57^\circ \times 4^\circ$ is shown here. With a limited number of reflectors, a large FOV can then be covered.

Index Terms: Silicon nanophotonics, integrated nanophotonics, free-space communication, waveguide devices.

1. Introduction

Optical retroreflectors provide a versatile way to allow localization and identification of objects or to transmit data using an extra modulating device. Light from a source illuminates the marker, and returns to it due to the action of the retroreflector. When used as a marker, optics have the inherent advantage of working at a small wavelength, allowing very precise localization of the markers, compared with radio frequency (RF) approaches. Furthermore, there is no problem of electromagnetic interference. However, we are limited by the line-of-sight (LOS) constraint and, typically, a limited field of view (FOV). When used as data transmission nodes (e.g., in sensor networks), the node typically consists of a bulk corner-cube reflector (CCR) or cat's-eye retroreflector (CERR), together with a transmissive or reflective modulator to impress the data on the retroreflective system. These systems then only require complexity at the base station for tracking the node and data processing, but the nodes can be kept quite simple, low cost, and lightweight. An example of such a system has been shown in [1], where a corner-cube array is used together with a liquid crystal modulator to transmit the data of the "smart dust motes" and most of the complexity is in the base station. An integrated approach to fabricate retroreflectors makes use of microelectromechanical systems (MEMS) technology. Such devices are typically useful for short-range applications [2].

In [3], a high contact-angle microdroplet is used to act as a retroreflector with possible applications in optical cross- and interconnects using photonic integration, while in [4], an integrated optical marker for simultaneous localization and identification of objects has been demonstrated. The main drawback in the latter was the limited FOV, which was solved by using a large number of reflectors, each looking in different directions.

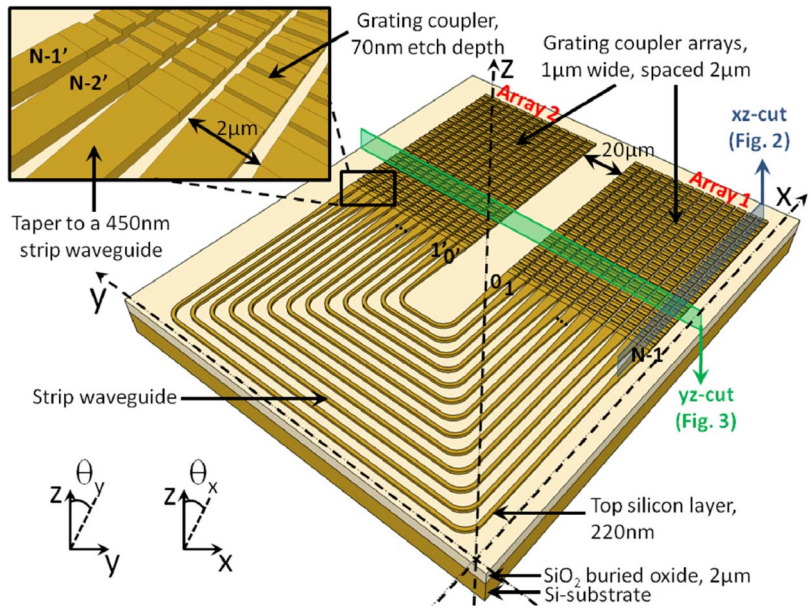

Fig. 1. Optical retroreflector on silicon-on-insulator.

In this paper, we describe the design and fabrication of a fully integrated retroreflector using the silicon photonics platform. This platform is complementary metal–oxide–semiconductor (CMOS) compatible and attracts a lot of interest for optical interconnects. In [5]–[7], this platform was used to fabricate a chip to free-space interface by using optical phased arrays which allow beam steering [8]. In this paper, a retroreflective structure is proposed as the interface between free-space and the chip. Such an integrated on-chip optical retroreflector has applications in chip-readout schemes, active alignment markers, or free-space cross- and interconnects. It could for example allow data communication between different on-chip photonic layers without the need for very sensitive alignment. In the current design, the retroreflector has a large FOV (of about 57°) in one dimension, while the FOV is still limited in the other dimension to about 4°. Only a limited number of retroreflectors is then needed to cover a large FOV. Achieving omnidirectional retroreflectivity is very challenging, especially for large angles with respect to the surface normal. By careful design, a FOV of $90^\circ \times 90^\circ$ around the surface normal can be covered with 20–25 retroreflectors. Due to the specific design, the retroreflectivity is wavelength dependent, which allows identification of the retroreflector. By integrating phase tuners, the reflected light can furthermore be modulated without the need of an external modulator. The proposed design can also act as a free-space optical demultiplexer when it is not retroreflecting.

In Section 2, we will discuss the working principle of the retroreflector. In Section 3, the fabrication of the component is described. Section 4 discusses the measurement setup, and in Section 5, the measurement results are given and discussed. Finally, a conclusion is given in Section 6.

2. Working Principle

Fig. 1 shows a schematic of the retroreflector design. We discuss the working principle of the retroreflector separately in the θ_x- and θ_y-direction.

2.1. θ_x-Direction

Light is coupled on- and off-chip using grating couplers. Grating couplers allow the coupling of light between an integrated circuit and an optical fiber [9] but act here as an interface between the integrated retroreflector and free-space. These grating couplers were designed to efficiently couple with the TE-like mode of the waveguides, and thus, for the remainder of this paper, it is assumed

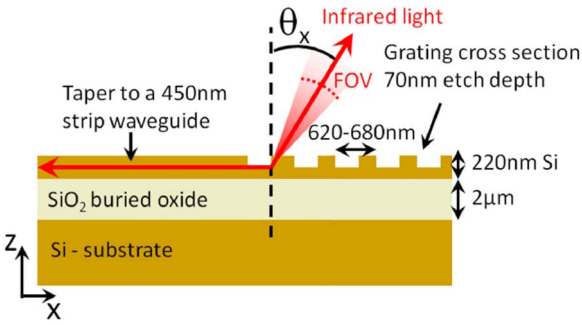

Fig. 2. Lateral cross section of the grating coupler (*xz*-cut of Fig. 1). Infrared light (red line) coming from a strip waveguide is coupled in/out using a grating coupler.

that all the light is TE polarized with respect to the retroreflector (main E-field component is E_y). A lateral cross-sectional view of the grating couplers is shown in Fig. 2. Infrared light coming from free-space impinges on the grating couplers and is coupled into the strip waveguide delay line based on the principle of diffraction. The light is then guided through the delay line and coupled off-chip again using a grating coupler at the other end of the delay line. As both grating couplers at each end of the delay line are the same, light couples out at the direction of incidence. Using the approach of [10], a grating can be designed that couples both TE- and TM-light into the negative and positive *x*-direction (see Fig. 2), respectively. When strip waveguide delay lines are then added at the other side of the grating, retroreflectivity can be observed for both polarizations.

The grating period determines the retroreflectivity in the θ_x-direction from the grating equation

$$\sin\,\theta_x = \frac{\Lambda_{gr} n_{eff,gr} - \lambda}{n_{ct}\Lambda_{gr}} \tag{1}$$

with Λ_{gr} the period of the grating, λ the free-space wavelength, $n_{eff,gr}$ the effective index of the guided mode in the grating area, and n_{ct} the refractive index of the background. By having a different grating period, the retroreflector will work at a certain, limited θ_x-range. Using different retroreflectors with different grating periods, we can increase the FOV in the θ_x-direction, as for a specific wavelength, a different retroreflector will light up depending on the angle of incidence θ_x. The beam width and FOV of the reflected light in the θ_x-direction depends on the out-coupling strength of the grating. As we are working with 70-nm-deep etched gratings, the grating strength is high, resulting in a short out-coupling length and, thus, a relatively large full-width at half-maximum (FWHM) beam width of about 3°–4°, which is then also the FOV of the retroreflector in the θ_x-direction.

2.2. θ_y-Direction

In Fig. 3, the transversal cross section of the grating coupler arrays is shown. This figure explains the operation principle of the retroreflector. Light that is coupled in using the grating coupler arrays is guided through delay lines and coupled back out through the same grating coupler arrays. Grating couplers $0, 1, \ldots, N-1$ are connected with grating couplers $0', 1', \ldots, N-1'$, respectively, using strip waveguide delay lines, as can be seen in Fig. 1. Assume a plane wave impinging on the retroreflector at grating coupler array 1 at an angle θ_y, as shown on the left side of Fig. 3. There is a phase delay $\Delta\Psi$ between adjacent grating couplers due to the angle of incidence θ_y. At a wavelength where the delay line difference corresponds to a phase difference of a multiple of 2π, this wavefront, with the corresponding phase delays, is copied to grating coupler array 2, as shown on the right side of Fig. 3. Light will then couple out at the angle of incidence θ_y, and retroreflectivity will be observed. For this wavelength, a plane wave that is coupled in through grating coupler array 1 will thus couple out through grating coupler array 2 at the same angle of incidence and *vice versa*.

The retroreflector is the optical analog of a radio-frequency (RF) Van Atta array antenna [11]. Such an array consists of equally spaced antennas that are interconnected by feeders of the same

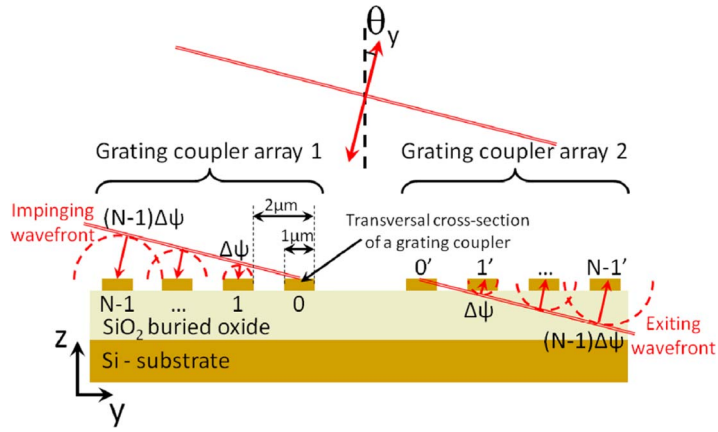

Fig. 3. Working principle of the retroreflector (*yz*-cut of Fig. 1). Grating couplers $0, 1, \ldots, N-1$ are connected with grating couplers $0', 1', \ldots, N-1'$. $\Delta\Psi$ is the phase delay of the impinging plane wave between adjacent grating couplers. The incoming wavefront is retroreflected in the same direction.

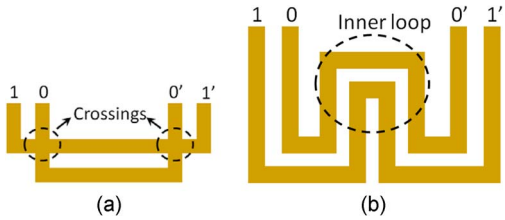

Fig. 4. Routing of the delay lines when all the delay lines need equal length. (a) Use of crossings. (b) Use of an extra inner loop.

length. The received RF signal is then retroreflected at the direction of incidence. For wavelength independent operation, the delay lines need to have an equal length. This can be done by using crossings as shown in Fig. 4(a) or by using an extra inner loop, as shown in Fig. 4(b). The former will result in high losses as a lot of crossings are needed, and the latter will make the retroreflector large as the size of the inner loop scales with the number of grating couplers.

The delay lines between the grating couplers will make the component wavelength dependent. Only when the delay length difference ΔL corresponds to a multiple of 2π phase difference, will retroreflectivity be observed

$$\frac{2\pi}{\lambda} n_{eff} \Delta L = m2\pi \tag{2}$$

with λ the free-space wavelength, n_{eff} the effective index of the delay lines, and m an integer, which is also called the order of the Arrayed Waveguide Grating (AWG) that is formed by these delay lines.

The retroreflector behavior in the θ_y-direction is investigated using a scalar approach. The FOV in the θ_y-direction is determined by the FOV of one grating coupler, which is determined by the width of the grating coupler. The full 1/e mode amplitude width in the *y*-direction of the fundamental TE-like mode of a 1-μm-wide grating coupler is simulated to be about 0.795 μm at 1550 nm and does not vary much with wavelength. It is this field that is coupled out by the grating coupler in the θ_y-direction. The FWHM of the far field of one such Gaussian is then 57°, which is the FOV of the retroreflector shown as the red dashed line in Fig. 5. Using a smaller grating coupler width will result in a larger FOV. The complete retroreflector is then simulated in the θ_y-direction as two arrays of 50 Gaussian with a 1/e width of 0.795 μm, spaced 2 μm and with an inner spacing of 20 μm, as shown in Figs. 1 and 3.

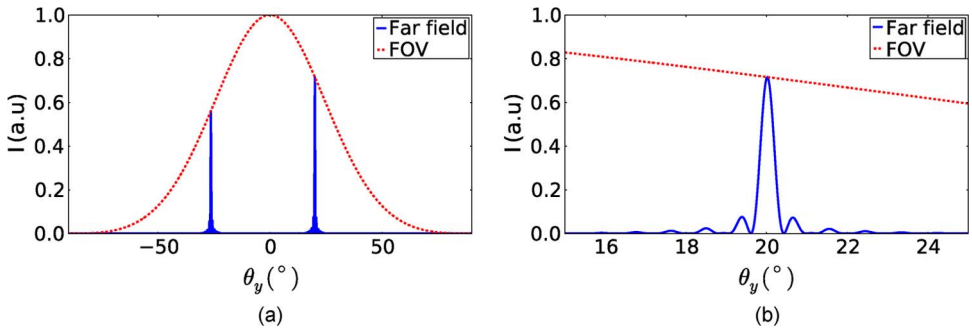

Fig. 5. (a) Simulated far field of the retroreflector for an impinging wave at $\theta_y = 20.0^\circ$ at $\lambda = 1523$ nm. The dashed line shows the far field of one grating coupler in the θ_y-direction being the FOV of the retroreflector in the θ_y-direction. (b) Magnification of (a) at the retroreflective angle.

A plane wave impinges on the structure and the overlap of the impinging fields with the grating coupler mode is calculated. These fields are then guided through the delay lines and couple back off-chip. The far field of all these (100) Gaussian profiles, taking into account their phase difference can then be easily calculated and is shown as the full blue line in Fig. 5. In Fig. 5, the structure is simulated for the case that condition (2) is fulfilled. The beam width of the retroreflected field is determined by the total size of the grating coupler arrays. The FWHM was simulated to be 0.33°. A second beam can also be seen in Fig. 5(a). This is not a retroreflected beam but is present due to the sampling of the radiated field. When having an array of radiating apertures, spaced at a distance Λ, different lobes are emitted at an angle of

$$\arcsin\frac{\lambda}{\Lambda} \tag{3}$$

with λ the free-space wavelength. In our case, this results in a lobe spacing of about 50° at $\lambda = 1523$ nm, which is the spacing visible in Fig. 5(a). This specific wavelength is chosen as it is (one of) the operating wavelengths of our retroreflectors given by (2).

When condition (2) is no longer fulfilled, the demultiplexing effect of the AWG comes into play. In Fig. 6, a close up of the far field is shown for different wavelength offsets $\Delta\lambda$. Two reflected lobes now arise which move away from the retroreflective direction for increasing wavelength offsets. If the detector only looks at the retroreflective angle, these lobes will quickly move away from the detector allowing precise localization and identification. The two lobes that are present correspond to the field emitted by grating coupler array 1 and 2 (see Fig. 3). Eventually, they will reach back to the same retroreflective direction when the condition (2) is again fulfilled, this time for another integer *m*, which occurs for a wavelength shift of $\Delta\lambda = 51$ nm.

3. Fabrication

The retroreflector shown Fig. 1 was fabricated on silicon-on-insulator (SOI) using standard CMOS processes [12], [13]. The buried oxide has a thickness of 2 μm, and the top silicon layer is 220 nm high. A deep etch of 220 nm is used to define the waveguides, while a shallow etch of 70 nm is used to etch the grating couplers. The delay lines have a width of 800 nm, apart from the bends which are tapered to a 450 nm width to allow very sharp bends, with a bend radius down to 3 μm. A waveguide width of 800 nm is used to reduce phase errors in the delay lines as a wide waveguide is more tolerant to fabrication errors. The length difference is the same for all retroreflectors and equal to 12 μm. These delay lines form an AWG. Finally, a benzocyclobutene (BCB) layer of about 700 nm is spun on top of the structure, and the structure is covered with a 500-nm gold layer, apart from the grating coupler areas. This reduces interference arising from diffuse reflected light from other parts of the chip.

The grating couplers have a width of 1 μm and are spaced 2 μm apart. The retroreflectors consist of two arrays of 50 grating couplers which are interconnected, as shown in Fig. 1. A cross section of

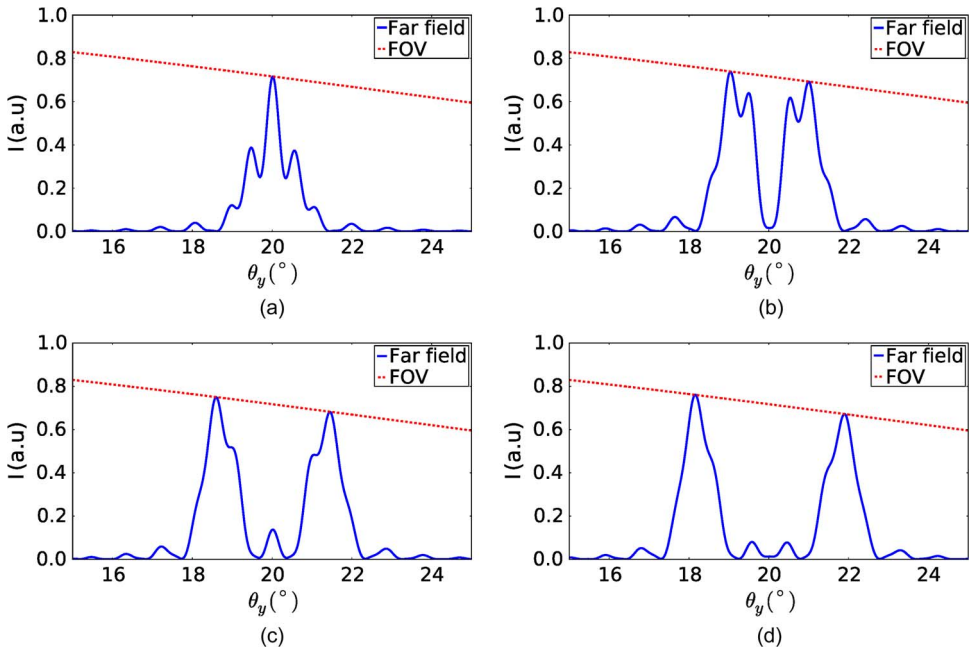

Fig. 6. Influence of the wavelength on the retroreflectivity in the θ_y-direction. (a) $\Delta\lambda = 0.5$ nm, (b) $\Delta\lambda = 1.0$ nm, (c) $\Delta\lambda = 1.5$ nm, and (d) $\Delta\lambda = 2.0$ nm, where $\Delta\lambda = |\lambda - \lambda_0|$, with λ_0 being the retroreflective wavelength.

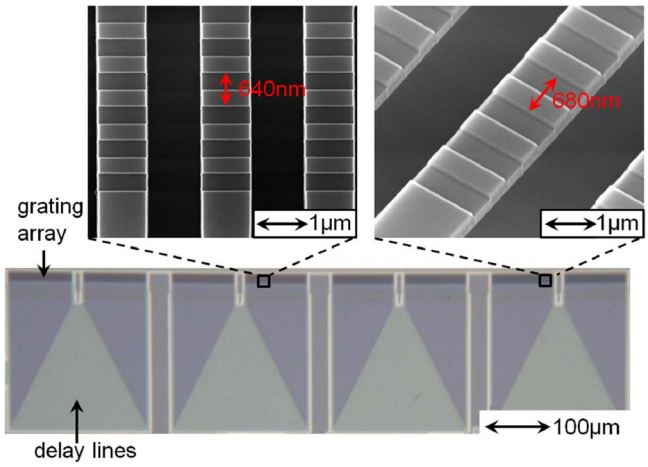

Fig. 7. Microscope image of the fabricated retroreflectors. Four different retroreflectors are shown with grating periods ranging from 620 nm (left) to 680 nm (right) in steps of 20 nm. Two SEM (Scanning Electron Microscope) magnifications of the grating couplers are shown as well.

these grating couplers is shown in Fig. 2. The gratings have a fill factor of 50%. Four different retroreflectors were fabricated with grating periods ranging from 620 nm up to 680 nm in steps of 20 nm, as shown in Fig. 7. The retroreflectivity for the different retroreflectors will thus occur at the same wavelength but at a different θ_x-angle due to the difference in grating period [see (1)].

4. Measurement Setup

The measurement setup is shown in Fig. 8. Light from a tunable laser passes through a polarization controller to a fiber collimator with a $1/e^2$ beam diameter of 7 mm. The collimated beam is then split through an infrared 3-dB plate beam splitter. Half of the light goes to the sample which is positioned

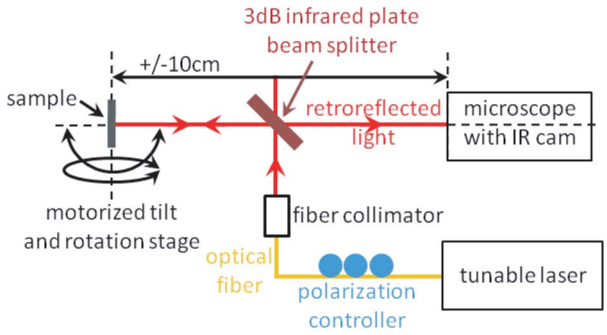

Fig. 8. Measurement setup to characterize the optical retroreflectors. The infrared light is split through a 3-dB splitter illuminating the sample. The sample is positioned in the center of a tilt and rotation stage. The reflected light is captured by a microscope with an infrared camera for different orientations of the sample.

in the rotation and tilt center of a motorized rotation and tilt stage. This large beam then illuminates different retroreflectors. The retroreflected light is then guided back to the 3-dB plate beam splitter, where half of the light will be captured by the microscope and infrared camera. When the light impinges perpendicularly on the structure, we get a large reflected beam due to specular reflection. By rotating and tilting the sample, the retroreflected light can be investigated. The numerical aperture (NA) of the microscope is about 0.1, meaning that we will measure the retroreflected light as long as the reflected light is in a cone with half-angle of 5.7° around the direction of incidence. More light than only the retroreflected light is captured, which is a limitation of our measurement setup. This can be solved by using a diaphragm to filter out nonretroreflective light.

5. Measurement Results and Discussion

First, the retroreflectivity measurements are discussed, then the efficiency with which light is coupled on/off the chip is investigated, and finally, we touch upon modulation possibilities of the component.

5.1. Retroreflectivity

In Fig. 9, the measured retroreflectivity is shown for different θ_x-angles. The four different retroreflectors operate at different θ_x-angles, while the wavelength is kept constant at 1523 nm. For this wavelength, (2) is fulfilled, and retroreflectivity is observed. In these images, the θ_y-angle is kept constant at 20°. We can clearly see the two grating coupler arrays of the retroreflectors lighting up at the same time.

In Fig. 10, the range for which retroreflectivity was measured is given. The chip was rotated to different θ_x- and θ_y-angles, and the image is then recorded. This image is then integrated and the result (normalized to 1) is shown as a color plot in Fig. 10. Each retroreflector works for a limited θ_x-range of about 4°, while the measured θ_y-range goes from 0° to 25° and, due to symmetry retroreflectivity, will be observed for a span of more than 50°, which compares with the theoretical FWHM span of 57°. When the θ_x- and θ_y-angle reaches 0°, the measurement is saturated by the specular reflection of the chip; therefore, these small angles are not shown in Fig. 10, but the influence of the specular reflection is still visible for small angles.

The retroreflectivity was observed for a wavelength range of about 5 nm around 1523 nm. This is because the NA of the microscope captures more light than only the retroreflected light. As the wavelength increases, two lobes arise moving away from the retroreflective direction, as shown in Fig. 6, but these two lobes are still captured by the microscope.

5.2. Power Efficiency

When used in optical marker applications, one is interested in the power efficiency of these markers, i.e., the amount of power that is coupled out of the grating couplers off-chip. Therefore,

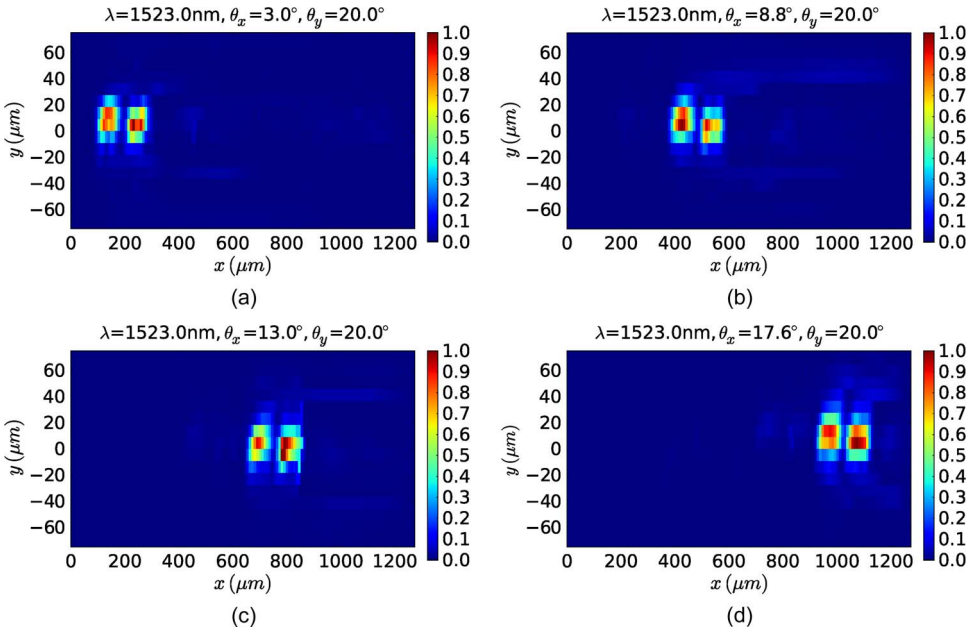

Fig. 9. Measured retroreflectivity at different θ_x-angles at $\lambda = 1523$ nm. The four different retroreflectors operate at the angles (a) $\theta_x = 3.0°$, (b) $\theta_x = 8.8°$, (c) $\theta_x = 13.0°$, and (d) $\theta_x = 17.6°$. The θ_y-angle is kept fixed at $\theta_y = 20.0°$.

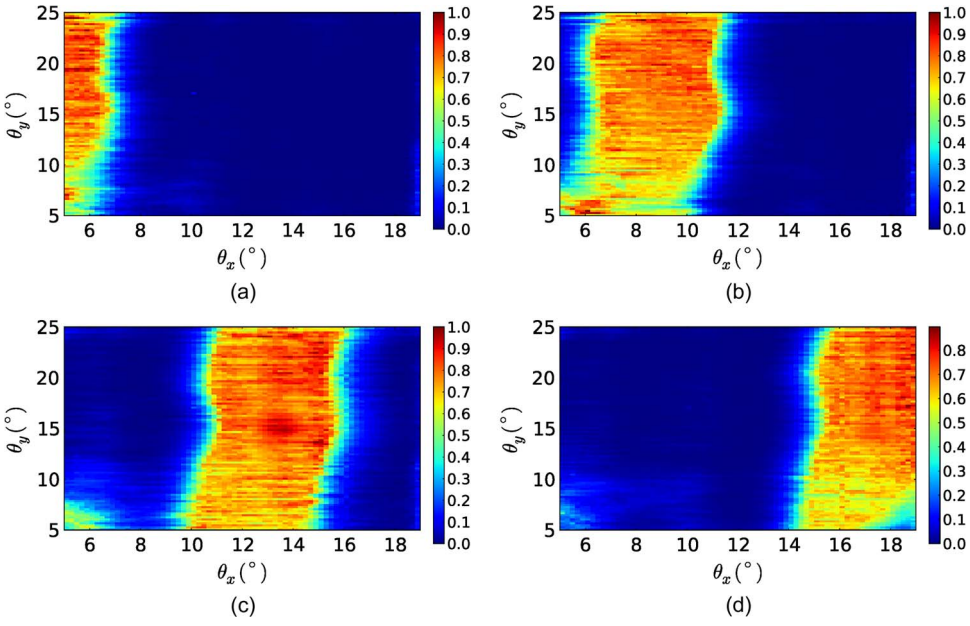

Fig. 10. Measured retroreflectivity range at $\lambda = 1523$ nm for four different retroreflectors. Each retroreflector works for a limited θ_x-range but a large θ_y-range. (a) $\Lambda_{gr} = 620$ nm, (b) $\Lambda_{gr} = 640$ nm, (c) $\Lambda_{gr} = 660$ nm, and (d) $\Lambda_{gr} = 680$ nm.

3-D-Finite Difference Time Domain (FDTD) simulations are performed to investigate the grating coupler efficiency as a function of wavelength [14]. The grating is excited with the fundamental TE-like mode, and the total power flux radiated away from the grating is calculated. The result is shown in Fig. 11. For a grating period of $\Lambda_{gr} = 620$ nm, there is a dip in the efficiency within the calculated spectral range. This dip is due to Bragg-coupling between the guided mode in the chip

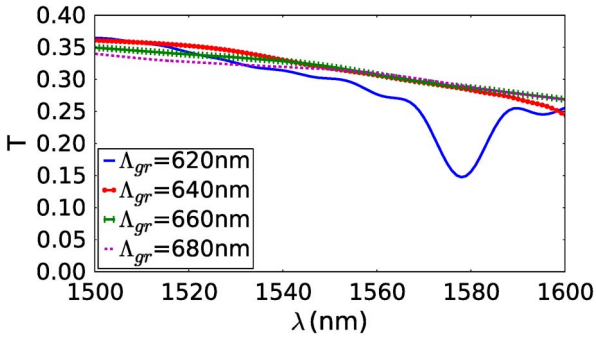

Fig. 11. Three-dimensional-FDTD simulated out-coupling efficiency of one grating coupler for different grating periods.

and a surface-normal diffraction order, as well as to the occurrence of second-order coupling between the guided mode and its backward mode. For the larger grating periods, this dip shifts to larger wavelengths and is no longer visible in the graph. The efficiency of the different gratings at the retroreflective wavelength $\lambda = 1523$ nm is similar for all retroreflectors and equal to about 34%. This efficiency can be increased by using a silicon overlay, which can boost the efficiency to more than 90% [15].

5.3. Modulation

These retroreflectors can be modulated on-chip to transmit data. The simplest method of modulation is to heat the chip. Silicon has a very high temperature coefficient $\partial n/\partial T = 1.84 \cdot 10^{-4}$ K^{-1} [16], [17]. By heating up the delay lines, (2) will no longer be fulfilled for the same wavelength, and the retroreflectivity will disappear, which we have measured experimentally by heating up the complete chip. The phase relation could also be destroyed using a liquid crystal [18] or nanoelectromechanical systems (NEMS) [19] approach. While these are relatively slow effects, a more practical approach is to integrate fast carrier-based modulators [20] within the retroreflector to destroy the phase relation between the delay lines and, thus, the retroreflectivity.

6. Conclusion

A retroreflector fabricated using the silicon photonics platform has been demonstrated. Each retroreflector has a FOV of $57^\circ \times 4^\circ$. A large range can thus be covered with only a limited number of retroreflectors. The retroreflector is wavelength dependent and acts as a free-space wavelength demultiplexer at the nonretroreflective wavelengths. By incorporating phase tuners to destroy the phase relation between the different grating couplers that couple light in and out of the retroreflector, the retroreflective data can be modulated, and data can be transmitted.

Acknowledgment

K. Van Acoleyen acknowledges the Research Foundation–Flanders (FWO) for a research grant. The authors acknowledge E. Lambert and W. Bogaerts for the LightPy Design Framework. The authors would like to thank S. Keyvaninia for the Scanning Electron Microscope (SEM) pictures.

References

[1] D. C. O'Brien, J. J. Liu, G. E. Faulkner, S. Sivathasan, W. W. Yuan, S. Collins, and S. J. Elston, "Design and implementation of optical wireless communications with optically powered smart dust motes," *IEEE J. Sel. Areas Commun.*, vol. 27, no. 9, pp. 1646–1653, Dec. 2009.

[2] P. G. Goetz, W. S. Rabinovich, R. Mahon, L. Swingen, G. C. Gilbreath, J. L. Murphy, H. R. Burris, and M. F. Stell, "Practical considerations of retroreflector choice in modulating retroreflector systems," in *LEOS Summer Topical Meeting Dig.*, New York, 2005, pp. 49–50.

[3] E. L. Landry, B. Born, G. Ross, and J. F. Holzman, "Integrated photonic retroreflectors for lateral cross-connects and interconnects," in *Proc. 23rd IEEE CCECE*, Calgary, AB, Canada, 2010, pp. 1–4.
[4] M. Verbist, W. Bogaerts, J. Schrauwen, and R. Baets, "Silicon-on-insulator-based retroreflective optical marker chips for simultaneous identification and localization," *IEEE J. Sel. Topics Quantum Electron.*, vol. 15, no. 5, pp. 1427–1431, Sep./Oct. 2009.
[5] K. Van Acoleyen, W. Bogaerts, J. Jágerská, N. Le Thomas, R. Houdré, and R. Baets, "Off-chip beam steering with a one-dimensional optical phased array on silicon-on-insulator," *Opt. Lett.*, vol. 34, no. 9, pp. 1477–1479, May 2009.
[6] K. Van Acoleyen, H. Rogier, and R. Baets, "Two-dimensional optical phased array antenna on silicon-on-insulator," *Opt. Exp.*, vol. 18, no. 13, pp. 13 655–13 660, Jun. 2010.
[7] K. Van Acoleyen, W. Bogaerts, H. Rogier, and R. Baets, "Two-dimensional dispersive beam steerer fabricated on silicon-on-insulator," in *Proc. 7th Int. Conf. GFP*, Beijing, China, 2010, pp. 371–373.
[8] P. F. McManamon, P. J. Bos, M. J. Escuti, J. Heikenfeld, S. Serati, H. K. Xie, and E. A. Watson, "A review of phased array steering for narrow-band electrooptical systems," *Proc. IEEE*, vol. 97, no. 6, pp. 1078–1096, Jun. 2009.
[9] G. Roelkens, D. Vermeulen, D. Van Thourhout, R. Baets, S. Brision, P. Lyan, P. Gautier, and J. M. Fedeli, "High efficiency diffractive grating couplers for interfacing a single mode optical fiber with a nanophotonic silicon-on-insulator waveguide circuit," *Appl. Phys. Lett.*, vol. 92, no. 13, pp. 131101-1–131101-3, Mar. 2008.
[10] D. Vermeulen, G. Roelkens, and D. Van Thourhout, "Grating structures for simultaneous coupling to TE and TM waveguide modes," U.S. Patent 20 100 322 555, Dec. 12, 2010.
[11] K. Nagai, "Van Atta array antenna device," U.S. Patent 3 731 313, May 1, 1973.
[12] ePIXfab, *The Silicon Photonics Platform,* 2011. [Online]. Available: http://www.epixfab.eu/
[13] S. K. Selvaraja, P. Jaenen, W. Bogaerts, D. Van Thourhout, P. Dumon, and R. Baets, "Fabrication of photonic wire and crystal circuits in silicon-on-insulator using 193-nm optical lithography," *J. Lightw. Technol.*, vol. 27, no. 18, pp. 4076–4083, Sep. 2009.
[14] A. F. Oskooi, D. Roundy, M. Ibanescu, P. Bermel, J. D. Joannopoulos, and S. G. Johnson, "MEEP: A flexible free-software package for electromagnetic simulations by the FDTD method," *Comput. Phys. Commun.*, vol. 181, no. 3, pp. 687–702, Mar. 2010.
[15] D. Vermeulen, S. Selvaraja, G. Verheyen, P. Lepage, W. Bogaerts, and G. Roelkens, "High-efficiency silicon-on-insulator fiber-to-chip grating couplers using a silicon overlay," in *Proc. 6th Int. Conf. GFP*, San Fransisico, CA, 2009, p. FPd1.
[16] J. Van Campenhout, W. M. J. Green, S. Assefa, and Y. A. Vlasov, "Integrated NiSi waveguide heaters for CMOS-compatible silicon thermo-optic devices," *Opt. Lett.*, vol. 35, no. 7, pp. 1013–1015, Apr. 2010.
[17] R. L. Espinola, M. C. Tsai, J. T. Yardley, and R. M. Osgood, "Fast and low-power thermooptic switch on thin silicon-on-insulator," *IEEE Photon. Technol. Lett.*, vol. 15, no. 10, pp. 1366–1368, Oct. 2003.
[18] W. De Cort, J. Beeckman, R. James, F. A. Fernandez, R. Baets, and K. Neyts, "Tuning silicon-on-insulator ring resonators with in-plane switching liquid crystals," *J. Opt. Soc. Amer. B, Opt. Phys.*, vol. 28, no. 1, pp. 79–85, Jan. 2011.
[19] K. Van Acoleyen, J. Roels, T. Claes, D. Van Thourhout, and R. Baets, "NEMS-based optical phase modulator fabricated on silicon-on-insulator," in *Proc. 8th Int. Conf. GFP*, London, U.K., 2011.
[20] N. N. Feng, S. R. Liao, D. Z. Feng, P. Dong, D. W. Zheng, H. Liang, R. Shafiiha, G. L. Li, J. E. Cunningham, A. V. Krishnamoorthy, and M. Asghari, "High speed carrier-depletion modulators with 1.4V-cm V pi L integrated on 0.25 mu m silicon-on-insulator waveguides," *Opt. Exp.*, vol. 18, no. 8, pp. 7994–7999, Apr. 2010.